Hindawi
Journal of Sensors
Volume 2023, Article ID 5568976, 20 pages
https://doi.org/10.1155/2023/5568976

Research Article

Based on Sliding Mode and Adaptive Linear Active Disturbance Rejection Control for a Magnetic Levitation System

Ziwei Wu,[1,2] **Kuangang Fan**,[1,2,3] **Xuetao Zhang**,[2,4] **and Weichao Li**[1,2]

[1]*School of Electrical Engineering and Automation, Jiangxi University of Science and Technology, Hongqi Street No. 86, Ganzhou 34100, China*
[2]*Magnetic Suspension Technology Key Laboratory of Jiangxi Province, Jiangxi University of Science and Technology, Hongqi Street No. 86, Ganzhou 34100, China*
[3]*Ganjiang Innovation Academy, Chinese Academy of Sciences, Academy of Sciences Street No. 1, Ganzhou 34100, China*
[4]*School of Mechanical and Engineering, Jiangxi University of Science and Technology, Hongqi Street No. 86, Ganzhou 34100, China*

Correspondence should be addressed to Kuangang Fan; kuangangfriend@163.com

Received 25 May 2023; Revised 10 August 2023; Accepted 20 September 2023; Published 31 October 2023

Academic Editor: Lihang Feng

The magnetic levitation system has evident advantages in reducing energy consumption, but its nonlinear characteristics increase the difficulty of control. This study proposes a control method that combines the improved particle swarm optimisation algorithm with sliding mode control and adaptive linear active disturbance rejection control (IPSO–SMC–ALADRC) to address the problems of weak anti-interference ability and stability in the application of traditional control methods in single-point magnetic levitation ball systems. First, a mathematical model of a single-point magnetic levitation ball is established. Second, the proportional and differential coefficients of LADRC are adjusted using adaptive laws, and the adaptive LADRC is combined with SMC to achieve stable control of the magnetic levitation ball. Moreover, an improved particle swarm optimisation algorithm is proposed to address the considerable number of adjustable parameters in the controller. The convergence and stability of the control algorithm were demonstrated using the Lyapunov equation. Finally, PID and LADRC are introduced for simulation and experimental comparison to verify the effectiveness of this control method. Results indicate that IPSO–SMC–ALADRC has excellent stability and anti-interference performance. This study addresses the problem of weak stability and anti-interference performance in the application of traditional control methods in the maglev system and further promotes the application of active disturbance rejection control in the magnetic levitation system.

1. Introduction

Magnetic levitation, as a new technology, has several advantages, such as friction-free, low power consumption, safety, and reliability [1, 2]. This technology has been widely used in a variety of industries, such as aerospace and transportation. However, realising effective suspension control of magnetic levitation is a major problem that must be addressed in engineering applications [3, 4]. On the one hand, the maglev system increases the difficulty of suspension control due to its instability, uncertainty, and high nonlinear characteristics. On the other hand, the magnetic levitation system is easily affected by external disturbances and changes in its own parameters. Consequently, how to realise its stable suspension control [5–7] has been a popular research topic amongst researchers. Ouyang et al. [8] proposed an adaptive linear active disturbance rejection method for magnetic levitation ball control based on the error elimination criteria, and it has achieved good dynamic performance but no experimental verification. Yu and Mu [9] introduced pure linear active disturbance rejection control (LADRC) to manage the magnetic suspension. This control method has excellent anti-disturbance performance. However, the parameter self-tuning of LADRC is not realised. Su et al. [10] proposed to apply ADRC to the control of single-point magnetic levitation balls. This control method has excellent stability, but it has not been verified through experiments. Su et al. [4] proposed a time-varying ADRC method to control a magnetic levitation ball. This control method has strong robustness, but it cannot achieve adaptive adjustment of parameters. Wei et al. [11] proposed an LADRC method based on the cuckoo algorithm to control the magnetic levitation ball. This method achieved excellent control accuracy, but no dynamic load test was carried out. Qinghua et al. [12] proposed an adaptive radial basis function control method. This control method does not idealise the controlled object and has excellent stability. However, the experimental verification does not introduce other control methods. Yang et al. [13] proposed an adaptive sliding mode control (SMC) with radial basis function neural network compensation and applied it to a magnetic levitation ball. Under this control mode, the magnetic levitation ball has almost no overshoot and exhibits good tracking performance, but it has not been verified through experiments. Ma et al. [14] proposed an RBF-PID control algorithm. The RBF-PID algorithm can not only make the magnetic levitation ball stable but also exhibit excellent applicability. However, the algorithm disregards the uncertainty of the model regarding the magnetic levitation ball. Yang et al. [15] proposed an adaptive SMC based on an RBF neural network (RBFNN) to solve the tracking control problem of magnetic levitation systems. The results show that the proposed controller exhibits fast convergence and robustness. However, selecting parameters during the controller design process is difficult. Zhang et al. [16] designed a particle swarm optimisation PSO–SMC–fuzzy PID control algorithm to minimise the chattering phenomenon in a magnetic levitation ball system. This approach not only minimises the chattering phenomenon in the magnetic levitation ball but also proves that the algorithm has strong robustness. However, the control performance of the magnetic levitation ball system declined. Wang et al. [17] proposed a maglev ball suspension control algorithm based on the combination of MPC + EIDSMO to minimise the control performance of a maglev ball due to external random uncertainties. The algorithm greatly improves the tracking performance of the magnetic levitation ball system, but its design is highly complex. Shen et al. [18] proposed a fuzzy neural network to compensate for the PID control algorithm, which not only made the control accuracy of the suspension ball less than approximately 0.4 mm but also made the system have a good adjustment time. Nonetheless, no corresponding experimental verification has been conducted. Wei et al. [19] proposed an improved AdaGrad optimal control algorithm, which makes the magnetic levitation ball system have good dynamic performance and robustness to a certain extent, but its delay time is relatively long. Sun et al. [20] proposed a supervisory control method based on RBFNN to achieve effective control of maglev vehicles. This method achieves excellent control performance in minimising random interference forces, flexible trajectories, and time delays in maglev vehicle systems. However, this method ignores the effect of different parameters on the controller design and stability. Sun et al. [21] proposed an adaptive SMC based on the minimum parameters of the RBF neural network. This control method has strong robustness but lacks experimental comparison. Sun et al. [22] proposed an adaptive neural network with robust position control, which can realise the high-precision control of a magnetic levitation orbit, but the theoretical analysis is not extensive. Lv and Long [23] proposed a nonlinear adaptive control algorithm to address the influence of external parameter changes in a maglev ball system. This algorithm requires no linearisation because the stable suspension control of a maglev ball can be realised. However, the influence of higher-order terms in the maglev ball system is ignored. Gao et al. [24] proposed a deep learning control algorithm that does not require complex parameter tuning of traditional PID controllers; hence, it has a better control effect than PID controllers. In different cases, the adaptability of this method and its application in a maglev train must be further studied. In literature [25], a projection recursion method based on adaptive backstepping control was proposed to adjust the position of the maglev ball in real-time by using a neural network. The proposed method exhibits precise and rapid tracking of the desired position of the maglev ball. However, the convergence rate of the maglev system will significantly decrease when the control signal (i.e., the suspended air gap value signal) greatly changes. In literature [26], a neural controller was developed and applied to regulate nonlinear and unstable maglev systems. Research shows that neural networks can be used as robust controllers for nonlinear and unstable systems and exhibit better performance than classical controllers. However, these networks require significant computational effort and analysis of complex time series. Li et al. [27] proposed a backstepping control method based on LESO to improve the control performance of the magnetic levitation system. This method efficiently addressed the challenge of achieving stable suspension of the magnetic levitation ball under uncertain conditions and realised high-precision tracking according to the actual suspension height. However, the algorithm is mainly reflected in the simulation of software and has not been integrated with an experimental platform. Liu and Zuo [28] proposed a fuzzy PID control algorithm independent of the precise mathematical model of the system to address the nonlinearity, hysteresis, and instability of the magnetic levitation system that the traditional control algorithm could not solve. The algorithm can realise the stable suspension of the magnetic levitation ball and has the advantages of high control precision and strong adaptive ability. However, the fuzzy rules required by this algorithm are highly complex and require extensive expertise experience. Gong and Li [29] adopted the strong learning method optimised by PSO to optimise and adjust the system parameters and address the issue of the poor dynamic performance that arises from traditional control of magnetic levitation systems. Although this algorithm has the advantage of strong robustness, it cannot effectively restrain the jitter problem caused by a maglev ball system. Literature [30] proposed a neural network controller for the trajectory tracking of a magnetic levitation system. This approach uses neural networks to approximate unknown parameters in the magnetic levitation system. Although the stability of the system is ensured, approximations for other parameters, such as nonmodeled dynamics and eddy currents, are neglected. Zhou et al. [31] applied active disturbance rejection control to the triaxial inertial stabilised platform of aerial remote sensing and achieved good control accuracy. However, their experimental and simulation projects did not achieve one-to-one corresponding. Humaidi et al. [32] combined the PSO algorithm with active disturbance rejection control to regulate the magnetic levitation ball system, resulting in improved dynamic performance of the controller. However, the aforementioned article did not address the problem that the PSO algorithm is susceptible to converging into local optimal solutions. Humaidi and Badr [33] proposed linear active disturbance rejection control and nonlinear active disturbance rejection control to regulate the position of a single-link flexible joint robot. This control mode has good anti-interference performance, but it has not applied the control mode to the actual robot system. Humaidi et al. [34] combined the PSO algorithm with the nonlinear active disturbance rejection control mode, which has excellent control accuracy, but it cannot achieve self-tuning of parameters.

In this study, we use the adaptive law for the proportional and differential term coefficients of linear active disturbance rejection control to realise the adaptive adjustment of parameters. Moreover, we combine adaptive linear active disturbance rejection control (ALADRC) with SMC to realise the stable control of the magnetic levitation ball system. We also introduce an IPSO algorithm to address the problem of an excessive number of adjustable parameters in the controller. This control method solves the problems of weak stability and anti-interference performance in the application of traditional control methods in magnetic levitation systems and further promotes the application of active disturbance rejection control in magnetic levitation systems. The remaining parts of this article are as follows: Section 2 specifies the nonlinear mathematical model of magnetic levitation balls. Section 3 introduces the designed IPSO-SMC-ALADRC control method, and provides theoretical derivation and analysis of the algorithm used. Section 4 conducted simulation and data analysis on the control mode. The control method was experimentally validated on the experimental platform in Section 5. Section 6 elaborates on the conclusions and directions for future work.

2. Single-Point Magnetic Levitation Ball Model

2.1. System Introduction. The single-point maglev system consists of a laser sensor, a steel ball, a power amplifier, and a control terminal. The operating principle of the equipment is as follows: first, the sensor senses the distance of the steel ball, converts the distance information into a voltage signal, and the voltage signal is inputted into the control terminal. The suitable control voltage is calculated by utilising the algorithm, and the control signal is converted into a more accurate current signal using the power amplifier. Finally, the current flows through the electromagnetic coil to generate an electromagnetic force, thereby achieving a balanced suspension. The direction of motion of the magnetic levitation ball is perpendicular to the ground. The schematic of the magnetic levitation ball system is shown in Figure 1.

2.2. Model of Magnetic Levitation Ball System. Before building the mathematical model of the maglev ball, the following assumptions need to be made:

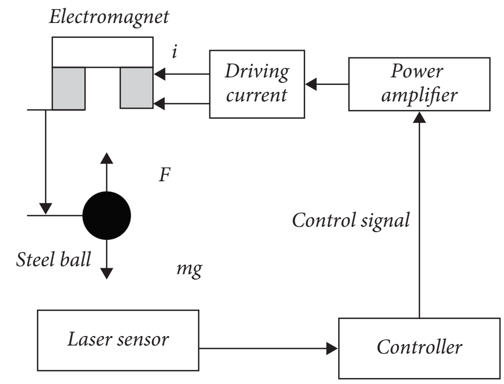

Figure 1: Schematic diagram of magnetic levitation system.

(1) Assume that there is no reluctance in the core.
(2) Assume that there is no magnetic leakage.
(3) Assume that the flux is uniformly distributed.

According to Figure 1, the nonlinear mathematical model of the magnetic levitation ball system can be expressed as follows:

$$\begin{cases} m\dfrac{d^2x(t)}{dt^2} = F(x,i) + mg, \\ F(x,i) = K\left(\dfrac{i}{x}\right)^2 = \dfrac{\mu_0 N^2 S}{4}\left(\dfrac{i}{x}\right)^2, \\ mg + F(i_0, x_0) = 0 \\ U(t) = Ri(t) + L_1\dfrac{di(t)}{dt} \end{cases} \tag{1}$$

where $F(i,x)$ is the magnet suction, and $F(i_0,x_0)$ is the magnet suction generated by the steel ball at the equilibrium point. According to Equation (1), the suction force of magnet $F(i,x)$ on the steel ball is increased using Taylor's formula at the equilibrium point (i_0,x_0):

$$F(x,i) = F(x_0,i_0) + k_i(i-i_0) + k_x(x-x_0) + oR(x), \tag{2}$$

where k_i is the stiffness coefficient for the current, and k_x is the stiffness coefficient for the suspension height. Therefore, the partial derivative of the electromagnetic suction at the equilibrium can be obtained as follows:

$$k_i = \frac{\partial F}{\partial i}\Big|_{(x_0,i_0)} = \frac{2Ki_0}{x_0^2} = \frac{\mu_0 N^2 S i_0}{2{x_0}^2}, \tag{3}$$

$$k_x = \frac{\partial F}{\partial x}\Big|_{(x_0,i_0)} = -\frac{2Ki_0}{x_0^3} = -\frac{\mu_0 N^2 S {i_0}^2}{2{x_0}^3}, \tag{4}$$

where $oR(x)$ is the higher-order term of the electromagnetic force. Given that the magnet suction is equal to the gravity of the steel ball at the equilibrium point, we have the following

Table 1: Parameters of the magnetic levitation ball system.

Variable and descriptions	Values
The mass of steel ball m(kg)	0.094
Coil turns N	2,450
Current in the coil at balance i_0(A)	0.5752
The suspension gap when the steel ball is balanced x_0(m)	0.01
Magnetic pole area $S(\mathrm{m}^2)$	$\pi\times 10^{-4}$
Permeability of vacuum μ_0(H/m)	$4\pi\times 10^{-7}$
Static inductance L_1(Hm)	135
Steel ball radius r(m)	0.0125
Coil resistance $R(\Omega)$	13.6

expression:

$$F(i_0, x_0) + mg = 0. \tag{5}$$

After ignoring the higher-order term, system Equation (1) can be rewritten as follows:

$$m\frac{d^2x}{dt^2} = k_i(i - i_0) + k_x(x - x_0). \tag{6}$$

Substituting Equations (3) and (4) into Equation (6) yields:

$$m\frac{d^2x(t)}{dt^2} = \frac{\mu_0 N^2 i_0 S}{2x_0^2} i - \frac{\mu_0 N^2 i_0^2 S}{2x_0^3} x. \tag{7}$$

Applying the Laplace transform to both sides of Equation (7) yields:

$$s^2X(s) = \frac{1}{m}\frac{\mu_0 N^2 \mathrm{i}_0 S}{2\mathrm{x}_0^2} I(s) - \frac{1}{m}\frac{\mu_0 N^2 i_0^2 S}{2\mathrm{x}_0^3} X(s). \tag{8}$$

The following expression is obtained because of the presence of a power amplifier in the single-point maglev ball system:

$$G_1(s) = \frac{U(s)}{I(s)} = K_\mathrm{a}. \tag{9}$$

Substituting Equation (9) into Equation (8), we have the following:

$$s^2X(s) = \frac{1}{m}\frac{\mu_0 N^2 i_0 S}{2x_0^2 K_a} U(s) - \frac{1}{m}\frac{\mu_0 N^2 i_0^2 S}{2x_0^3} X(s). \tag{10}$$

According to Equation (10), the transfer function of the single-point maglev ball system can be expressed as follows:

$$G(s) = \frac{\frac{1}{m}\frac{\mu_0 N^2 i_0 S}{2x_0^2 K_a}}{s^2 + \frac{1}{m}\frac{\mu_0 N^2 i_0^3 S}{2{X^3}_0}}. \tag{11}$$

Let $x = x_1$, $\dot{x}_1 = x_2$, $y = x_1$, The expression for the model of a magnetic levitation ball is as follows:

$$\begin{cases} \dot{x}_1 = x_2 \\ \dot{x}_2 = d(t) + b_0 u\,, \\ y = x_1 \end{cases} \tag{12}$$

where x_1 is the levitation height of the magnetic levitation ball, x_2 is the movement speed of the magnetic levitation ball, and $d(t)$ is the total disturbance to the system.

Remark 1. Currently, two methods are used to establish magnetic levitation ball models. The first one is to obtain a linear mathematical mapping model of the magnetic levitation ball through nonlinear coordinate transformation. The other one is to ignore the higher-order term of the electromagnetic force at the equilibrium point of the magnetic levitation ball to obtain its mathematical model. The advantage of establishing a mathematical model through coordinate transformation is that the simulation results are more similar to the actual results. The disadvantage is that the control method used has more adjustable parameters, and the workload of parameter adjustment is greater. The advantage of ignoring higher-order modelling methods is that establishing mathematical models is more convenient, and more effective control methods can be used to regulate magnetic levitation balls. The disadvantage is that some errors may occur during simulation and practical applications. This study adopts a modelling method that ignores higher-order terms.

The parameter values and physical meanings of the actual model of the magnetic levitation ball system are shown in Table 1.

3. Controller Design

In this work, SMC is combined with adaptive linear active disturbance rejection control to improve the stability of the controller. An adaptive law with two parameters is designed

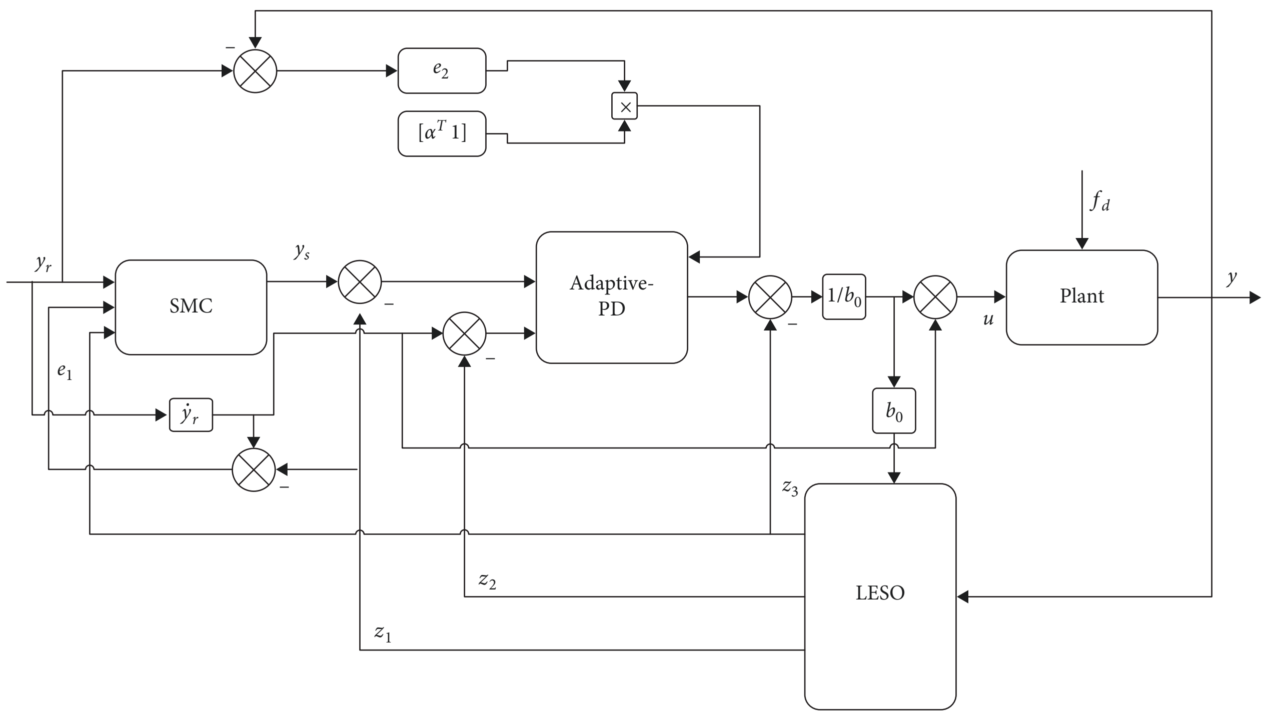

Figure 2: Control structure block diagram of SMC–ALADRC.

based on the principle of error elimination for the proportional coefficient k_p and differential coefficient k_d of PD module in LADRC. Furthermore, debugging by means of the approximation method is impossible because of the excessive number of adjustable parameters in the controller. Accordingly, the IPSO algorithm is introduced to confirm the parameters in the controller. The specific control structure is shown in Figure 2.

3.1. Sliding Mode Control Design. SMC can improve the robustness of the controller and the control precision of LADRC. The sliding surface can be designed as follows:

$$s = w_1 e_1 + \dot{e}_1, \tag{13}$$

where w_1 is the scalar design parameter, $e_1 = z_1 - y_r$ is the error between the input and the output signals of the linearly extended state observer, and y_r is the input signal of the system.

$$\dot{s} = w_1 \dot{e}_1 + \ddot{e}_1 = w_1 \dot{e}_1 + \ddot{z}_1 - \ddot{y}_r. \tag{14}$$

As z_1 is the evaluation value of the suspension height x_1 of the steel ball, z_2 is the evaluation value of the movement speed x_2 of the steel ball, z_3 is the evaluation value of the total disturbance $d(t)$ of the system, and $\ddot{x}_1 = \dot{x}_2 = d(t) + b_0 u$, Equation (14) can be expressed as follows:

$$\dot{s} = w_1 \dot{e}_1 + \ddot{e}_1 = w_1 \dot{e}_1 + z_3 + b_0 u - \ddot{y}_r. \tag{15}$$

SMC control law y_s can be expressed as follows based on the characteristics of SMC:

$$y_s = y_{\text{seq}} + y_{\text{ssw}}, \tag{16}$$

where y_{seq} is the equivalent part, and y_{ssw} is the switching part, and its expression is expressed as follows:

$$y_{\text{seq}} = \ddot{y}_r - w_1 \dot{e}_1 - z_3 \tag{17}$$

$$y_{\text{ssw}} = -w_2 s, \tag{18}$$

where w_2 is the scalar design parameter. The SMC control law can be expressed as follows:

$$y_s = \ddot{y}_r - w_1 \dot{e}_1 - z_3 - w_2 s. \tag{19}$$

3.2. Design of LADRC. The mathematical expression of the control voltage is as follows:

$$u = k_p (y_s - z_1) + k_d (\dot{y}_r - z_2) + \ddot{y}_r - \frac{z_3}{b_0}, \tag{20}$$

where k_p and k_p represent the proportional and differential coefficients, respectively; b_0 is the tunable gain; u is the control input; y_s is the output signal of SMC and the input signal of the LADRC controller; z_1, z_2 and z_3 represent LESO's evaluation status of the controlled object, and they evaluate the ball's suspension height x_1, the ball's moving speed x_2 and the total disturbance, respectively, which can designed as follows:

$$\begin{cases} \dot{z}_1 = z_2 + \beta_1(y - z_1) \\ \dot{z}_2 = z_3 + \beta_2(y - z_1) + b_0 u, \\ \dot{z}_3 = \beta(y - z_1) \end{cases} \tag{21}$$

where $\beta = [\beta_1, \beta_2, \beta_3]^T$ is the gain vector of LESO, and y is the output of the system, which is the actual suspension height.

Remark 2. LESO is the most important part of a LADRC controller. It mainly regards the total disturbance received by the system as a new state variable and the input and output of the controlled object as the input of the linear extended state observer, through which the state variable of the control system is evaluated.

LESO's characteristic equation can be expressed as follows:

$$D(s) = s^3 + \beta_1 s^2 + \beta_2 s + \beta_3 = (s + \omega_o)^3, \tag{22}$$

where $\beta = [3\omega_o\ 3\omega_o^2\ \omega_o^3]$, and ω_o is the observation bandwidth.

The initial control voltage u_0 output by the PD module can be expressed as follows:

$$u_0 = k_p(y_s - z_1) + k_d(\dot{y}_r - z_2) + \ddot{y}_r. \tag{23}$$

3.3. Design of LADRC Adaptive Law. The expression of the k_p and k_d parameter adaptive law proposed in literature [35] is as follows:

$$\dot{\widehat{k}}_p = [\delta k_p(y_s - z_1)\vartheta]/\widetilde{k}_p \tag{24}$$

$$\dot{\widehat{k}}_d = [\delta k_d(\dot{y}_r - z_2)\zeta]/\widetilde{k}_d, \tag{25}$$

where ϑ and ζ are adjustable parameters. δ is the error filter, and it can be expressed as follows:

$$\delta = [\alpha^T \quad 1]e_2. \tag{26}$$

The error $e_2 = y - y_r$ is determined according to the input and output signals of the system. where is the appropriate coefficient $\alpha = t_1$. When $\delta \longrightarrow 0$, it satisfies $e_2 \longrightarrow 0$.

Take the derivative of δ to obtain:

$$\dot{\delta} = \dot{x}_2 - \ddot{y}_r + [0 \quad \alpha^T]e_2 = -a\delta + k_p(y_s - z_1) + k_d(\dot{y}_r - z_2) \tag{27}$$

Remark 3. To eliminate the singularity in the adaptive law of Equations (24) and (25), the problem that $\tilde{k}_p$ and $\tilde{k}_d$ are equal to zero. The integral form of $\dot{\widehat{k}}_p$ and $\dot{\widehat{k}}_d$ can be written as an adaptive law, expressed as follows:

$$\widehat{k}_p = \int_0^t [\delta k_p(y_s - z_1)\vartheta]/\widetilde{k}_p d\tau + k_{p0}, \tag{28}$$

$$\widehat{k}_d = \int_0^t [\delta k_d(y_r - z_2)\zeta]/\widetilde{k}_d d\tau + k_{d0}, \tag{29}$$

where $\widehat{k}_p$ and $\widehat{k}_d$ are the estimated values of proportional term coefficient k_p and differential term coefficient k_d in LADRC. We choose the appropriate parameters (k_{p0} and k_{d0}) to ensure that $\tilde{k}_p = k_p - \widehat{kp}$ and $\tilde{k}_d = k_d - \widehat{kd}$ are not equal to zero.

3.4. Improved Particle Swarm Optimisation. The controller cannot be debugged through experience due to the presence of a considerable number of adjustable parameters. Therefore, we introduce an improved particle swarm intelligence algorithm to optimise the controller parameters: $b_0, \omega_o, k_{p0}, k_{d0}, \alpha, \zeta, \vartheta, k_p$, and k_d.

Remark 4. Choosing an appropriate compensation gain b_0 is crucial in improving the dynamic performance of the system. In this study, an IPSO algorithm was used to confirm the parameter value.

Constraint factors were used to improve the convergence speed based on the particle swarm algorithm. A simulated annealing operation was introduced, and the temperature was set based on the initial state of the population. Meanwhile, the Metropolis criterion and temperature guidance were used to guide the population to accept differential solutions with a certain probability. Accordingly, the local convergence problems were addressed, and the parameter optimisation accuracy was improved. The particle velocity and position update rules in the PSO algorithm that introduces constraint factors are as follows:

$$\begin{cases} V_{ij}(k+1) = \rho V_{ij}(k) + c_1 r_1 \left(\mathrm{Pbest}_{ij} - X_{ij}(k)\right) + c_2 r_2 \left(\mathrm{gbest}_{ij} - X_{ij}(k)\right) \\ X_{ij}(k+1) = X_{ij}(k) + V_{ij}(k+1) \end{cases} \tag{30}$$

$x_{ij}(k)$ and $v_{ij}(k)$ represent the jth dimensional position component and velocity component of the ith particle at time k, respectively; c_1 and c_2 are the cognitive and population factors, respectively; r_1 and r_2 are the random factors between [0,1]; The best position component in the jth dimension that the ith particle and all particles currently pass through, respectively; ρ is the constraint factor, and its specific form is as follows:

$$\begin{cases} \rho = \dfrac{2}{\left|2 - \varphi - \sqrt{\varphi^2 - 4\varphi}\right|}. \\ \varphi = c_1 + c_2 \end{cases} \tag{31}$$

We choose ITAE as the fitness function:

$$J_{\mathrm{ITAE}} = \int_0^{\infty} t|e(t)|dt. \tag{32}$$

The process of IPSO optimisation algorithm tuning the SMC–ALADRC controller parameters is shown in Figure 3, and the main steps are as follows:

Step 1: Initialise the speed and position of each particle. Calculate the fitness of each particle according to the fitness function Equation (32) and determine the optimal particle position of the initial population.

Step 2: Execute the IPSO algorithm to update the speed and position of each particle using Equations (30) and (31). Calculate the fitness of each particle and update the individual optimal position and the population optimal position according to the fitness. If the IPSO algorithm converges, then proceed to the next step; otherwise, repeat Step 2.

Step 3: Introduce the simulated annealing algorithm and set its initial position as the optimal position of the current PSO population. Moreover, randomly select a new position within the algorithm domain and guide the population to accept the different solutions with a certain probability through the Metropolis criterion and temperature guidance.

Step 4: If the fitness of the final position of the simulated annealing algorithm is less than that of the current population's most favourable position of the IPSO algorithm, then it will be taken as the new population's optimal position of the IPSO algorithm. The annealing temperature will be updated. The update formula is: $Te(k+1) = Te(k) * \text{lamda}$;

The following figure compares the fitness function convergence curve of the IPSO algorithm with that of the traditional PSO algorithm.

Figure 4(a) shows that traditional PSO algorithms require approximately 40 iterations to converge. Figure 4(b) demonstrates that the improved particle swarm algorithm can converge after approximately 20 iterations. The improved particle swarm algorithm has a low fitness value. This finding indicates that the IPSO has faster convergence speed and search accuracy.

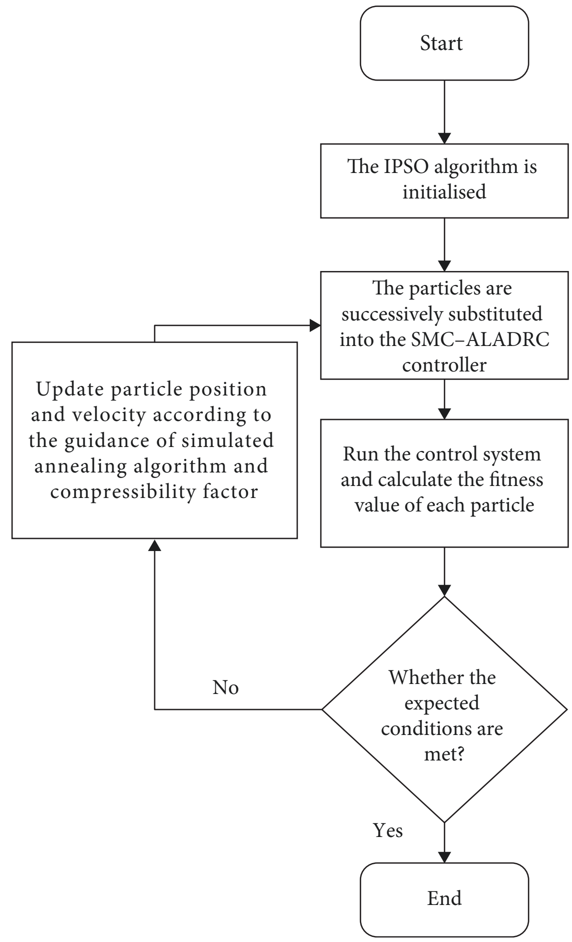

Figure 3: Optimization flow chart by improved particle swarm optimisation algorithm.

3.5. Theoretical Verification

Assumption 1. *The signals of the system converge, and the errors of the system are all equal to zero.*

In the following, we will use Lyapunov to prove the convergence and stability of adaptive laws. The Lyapunov function is designed as follows:

$$V = \frac{1}{2}s^2 + \frac{1}{2}\delta^2 + \frac{1}{2}\tilde{k}_p \vartheta \tilde{k}_p + \frac{1}{2}\tilde{k}_d \zeta \tilde{k}_d. \tag{33}$$

It is known that V is positively definite. Take the derivative of the above formula:

$$\dot{V} = s\dot{s} + \delta\dot{\delta} + \tilde{k}_p \vartheta \dot{\tilde{k}}_p + \tilde{k}_d \zeta \dot{\tilde{k}}_d. \tag{34}$$

Substituting Equations (22) and (27) into Equation (34) yields:

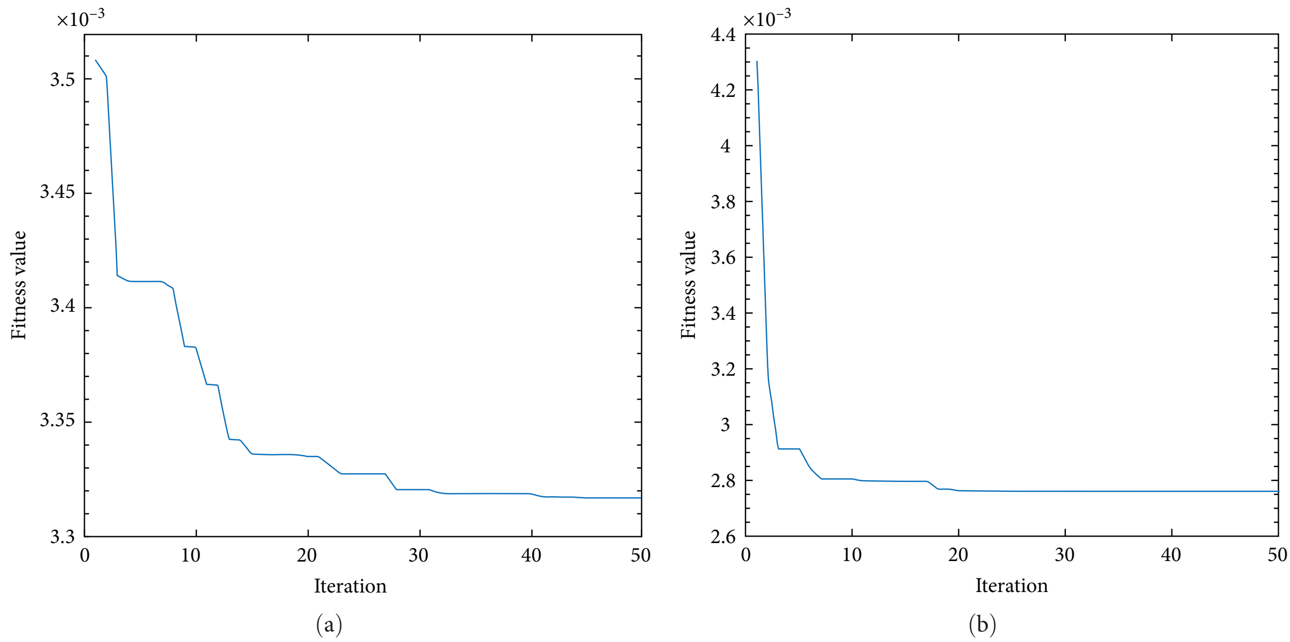

FIGURE 4: The convergence curve of Sparrow search algorithm fitness function: (a) convergence curve before algorithm improvement; (b) convergence curve after algorithm improvement.

$$\begin{aligned}\dot{V} &= s(w_1\dot{e}_1 + \ddot{e}_1) + \delta\left[-a\delta + k_p(y_s - z_1) + k_d(\dot{y}_r - z_2)\right] + \tilde{k}_p\vartheta^{-1}\dot{\tilde{k}}_p + \tilde{k}_d\zeta^{-1}\dot{\tilde{k}}_d \\ &= s(w_1\dot{e}_1 + \ddot{z}_1 - \ddot{y}_r) - a\delta^2 + \delta k_p(y_s - z_1) + \delta k_d(\dot{y}_r - z_2) + \tilde{k}_p\vartheta^{-1}\dot{\tilde{k}}_p + \tilde{k}_d\zeta^{-1}\dot{\tilde{k}}_d \\ &= s(w_1\dot{e}_1 + z_3 + y_s - \ddot{y}_r) - a\delta^2 + \delta k_p(y_s - z_1) \\ &\quad + \delta k_d(\dot{y}_r - z_2) + \tilde{k}_p\vartheta^{-1}\dot{\tilde{k}}_p + \tilde{k}_d\zeta^{-1}\dot{\tilde{k}}_d.\end{aligned} \tag{35}$$

Substituting Equation (23) into the above formula yields:

$$\begin{aligned}\dot{V} &= s(w_1\dot{e}_1 + z_3 + \ddot{y}_d - w_1\dot{e}_1 - z_3 - w_2 s - \ddot{y}_r) + \delta\left[-a\delta + k_p(y_s - z_1) + k_d(\dot{y}_r - z_2)\right] + \tilde{k}_p\vartheta^{-1}\dot{\tilde{k}}_p + \tilde{k}_d\zeta^{-1}\dot{\tilde{k}}_d \\ &= s(w_1\dot{e}_1 + \ddot{z}_1 - \ddot{y}_r) - a\delta^2 + \delta k_p(y_s - z_1) + \delta k_d(\dot{y}_r - z_2) + \tilde{k}_p\vartheta^{-1}\dot{\tilde{k}}_p + \tilde{k}_d\zeta^{-1}\dot{\tilde{k}}_d \\ &= s(w_1\dot{e}_1 + z_3 + y_s - \ddot{y}_r) - a\delta^2 + \delta k_p(y_s - z_1) + \delta k_d(\dot{y}_r - z_2) + \tilde{k}_p\vartheta^{-1}\dot{\tilde{k}}_p + \tilde{k}_d\zeta^{-1}\dot{\tilde{k}}_d.\end{aligned} \tag{36}$$

Equations (24) and (25) are substituted into the above formula to obtain the following:

$$\begin{aligned}\dot{V} &\le -w_2 s^2 - a\delta^2 + \delta k_p(y_s - z_1) + \delta k_d(\dot{y}_r - z_2) - \tilde{k}_p\vartheta^{-1}\left[\delta k_p(y_s - z_1)\vartheta\right]/\tilde{k}_p - \tilde{k}_d\zeta^{-1}\left[\delta k_d(\dot{y}_r - z_2)\zeta\right]/\tilde{k}_d \\ &\le -w_2 s^2 - a\delta^2 + \delta k_p(y_s - z_1) + \delta k_d(\dot{y}_r - z_2) \\ &\quad - \delta k_p(y_s - z_1) - \delta k_d(\dot{y}_r - z_2).\end{aligned} \tag{37}$$

Simplifying the above formula yields:

$$\dot{V} \le -w_2 s^2 - a\delta^2, \tag{38}$$

where w_2 and a are the positive parameters. The above formula can be written as follows:

$$\dot{V} \leq 0. \tag{39}$$

It can be seen that $\dot{V}$ is negative definite, and because there is $V \longrightarrow \infty$ when $\|s\| \longrightarrow \infty$ and $\|\delta\| \longrightarrow \infty$ exist, according to Lyapunov's theorem, it can be concluded that the system is asymptotically stable over a large range at the coordinate origin.

From Equation (39), it can be concluded that the Lyapunov equation is bounded. According to Barbarat theorem, we can obtain:

$$\lim_{t \longrightarrow \infty} s(t) = 0, \lim_{t \longrightarrow \infty} \delta(t) = 0. \tag{40}$$

By Lyapunov theory $\tilde{k}_p$ and $\tilde{k}_d$ are bounded, the error between the input signal and the input signal it is also bounded and approaches zero, and all signal of system are bounded.

4. Simulink Result

We set the parameters of PID and LADRC in the same optimisation conditions to ensure the fairness of the simulation test and conduct the simulation test with IPSO–SMC–ALADRC. The following figure shows the convergence curve of the fitness function of the three control modes.

Figure 5(a)–5(c) demonstrate that the fitness value of PID eventually converges to 3.389×10^{-2}, LADRC converges to 1.112×10^{-2}, and IPSO–SMC–ALADRC converges to 4.188×10^{-3}. The fitness value of SMC–ALADRC decreases by 87.64% and 62.34% compared with those of PID and LADRC, respectively. Therefore, after IPSO, SMC–ALADRC has better dynamic performance than PID and LADRC.

The following simulation tests are primarily conducted to verify the anti-disturbance performance of the three control modes. We use three error indicators to test the anti-disturbance ability of the three control methods. The three error indicators are IAE, ITAE, and ITSE. The expressions of the three indicators are as follows:

$$\mathrm{IAE} = \int_0^t |e_y| d\tau = \int_0^t |y_r - y_{\mathrm{out}}| d\tau, \tag{41}$$

$$\mathrm{ITAE} = \int_0^t t|e_y| d\tau = \int_0^t t|y_r - y_{\mathrm{out}}| d\tau, \tag{42}$$

$$\mathrm{ITSE} = \int_0^t t|e_y| d\tau = \int_0^t t(y_r - y_{\mathrm{out}})^2 d\tau, \tag{43}$$

where y_r is the set suspension height, and y_{out} is the actual suspension height.

The following tests were conducted by introducing PID, LADRC, and IPSO–SMC–ALADRC:

(1) Step signal testing.

(2) Anti-interference test.

(3) Error testing.

The specific parameters of the three controllers in the simulation are shown in Table 2.

4.1. Step Response. The effectiveness of the three control methods is verified by comparison. From Figure 6(a), it can be seen that although PID control has the advantages of simple operation and fast response, its overshoot is quite large, and the time to reach a stable suspension position is very long (up to 1.860 s). The regulation time of LADRC to achieve a stable suspension is shorter than that of PID, and its regulation time reaches 0.604 s. However, the overshoot is considerably large. Meanwhile, only IPSO–SMC–ALADRC can meet the shortcomings of both approaches. The shortest regulation time also has the smallest overshoot, and its regulation time is 0.323 s. The adjustment time of IPSO–SMC–ALADRC has decreased by 82.63% and 46.52% compared with those of PID and LADRC. At the overshoot level, the overshoot of PID is 10.52%, LADRC is 35.62%, and IPSO–SMC–ALADRC is 3.42%. Figure 6(b) demonstrates that the control voltage adjustment times of PID, LADRC, and IPSO–SMC–ALADRC are 1.495, 0.434, and 0.298 s, respectively. The adjustment time required for IPSO–SMC–ALADRC to reach a stable state of control voltage has decreased by 86.67% and 31.34% compared with those of PID and LADRC, respectively.

The error indicators of IAE, ITAE, and ITSE of IPSO–SMC–ALADRC have decreased by 93.41%, 87.64%, and 75.46% compared with that of PID, respectively. The error indicators of IAE, ITAE, and ITSE of IPSO–SMC–ALADRC have decreased by 84.93%, 62.34%, and 23.34% compared with that of LADRC, respectively. Based on the simulation results and data level, IPSO–SMC–ALADRC has better dynamic performance. The specific error values are shown in Table 3.

4.2. Analysis of Anti-Interference Performance. We used different levels of interference to interfere with the control system and demonstrate the anti-interference performance of the three control methods. The following figure shows the error trend of the three control methods under different intensities of interference.

Figure 7(a)–7(c) shows the changes in the three error criteria of the three control modes when the interference load increases. The errors of IPSO–SMC–ALADRC are far less than those of the other two control modes, and those of PID and LADRC significantly increase when the disturbance increases. Only the error of IPSO–SMC–ALADRC is in a relatively stable state, indicating that it has better anti-interference performance. The interference applied to the system in this study is pulse signal interference, whose amplitude is determined by the required interference force, and the interference duration is limited to 0.01 s.

We choose the three control modes of the $f_d = 5\,N$ and $f_d = 10\,N$ interference loads for comparison to more intuitively reflect the disturbance resistance of the three control modes. The specific effect is shown in Figure 8.

When the interference is 5 N, the distances of PID, LADRC, and IPSO–SMC–ALADRC deviating from the equilibrium position are 0.984, 1.021, and 0.144 mm, respectively, as shown in Figure 8(a). When the interference is 5 N,

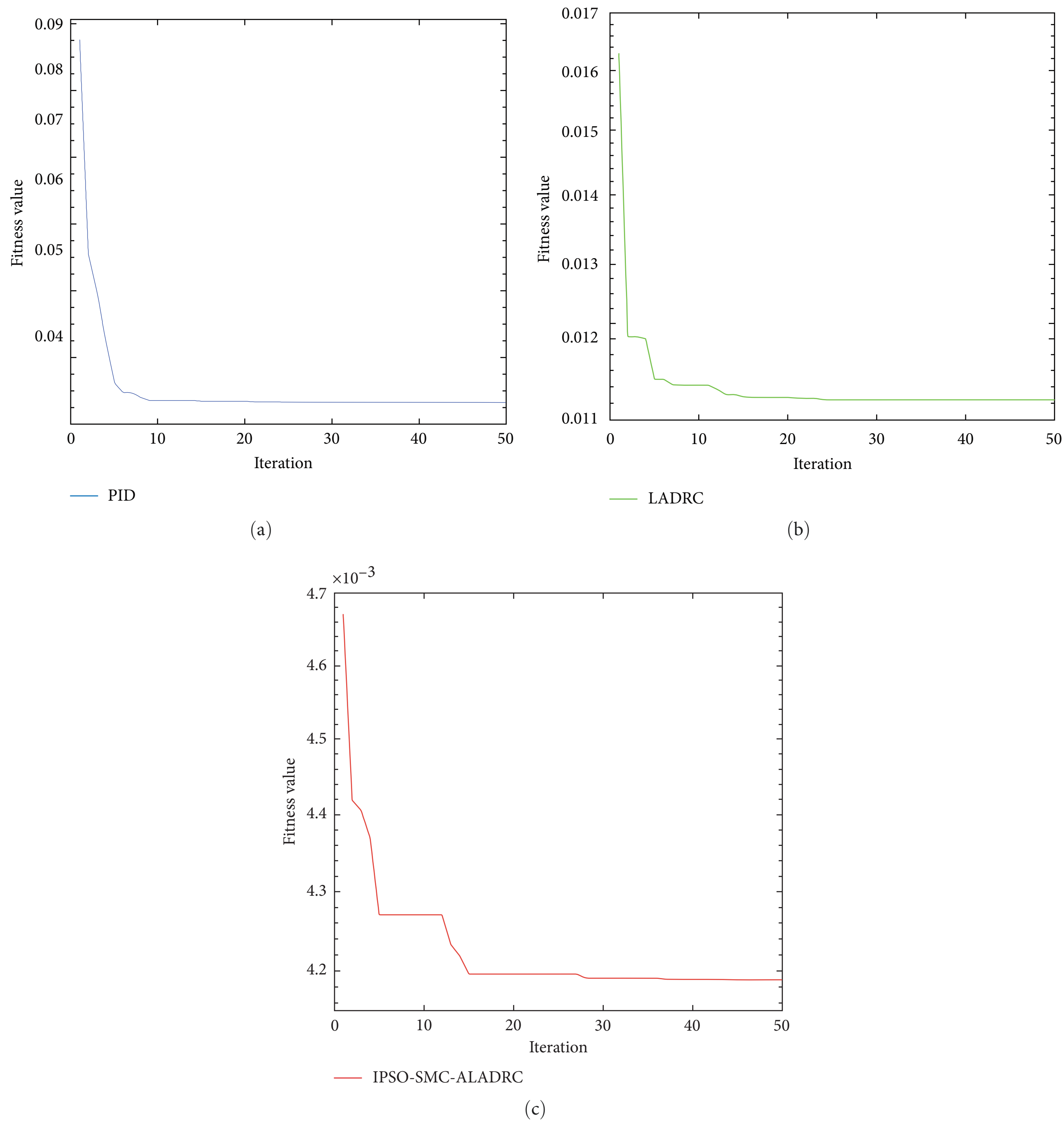

Figure 5: Fitness function convergence curve: (a) convergence curve of PID fitness function; (b) convergence curve of LADRC fitness function; (c) convergence curve of IPSO–SMC–ALADRC fitness function.

IPSO–SMC–ALADRC reduces the distance from the equilibrium position by 85.37% and 84.13% compared with those of PID and LADRC, respectively. Figure 8(b) shows that the control voltage fluctuations of PID, LADRC, and IPSO–SMC–ALADRC were 0.176, 0.301, and 0.092 V, respectively, after adding 5 N interference. The control voltage fluctuations of IPSO–SMC–ALADRC after interference decreased by 47.73% and 69.44% compared with those of PID and LADRC, respectively. When the interference is 10 N, the distances of PID, LADRC, and IPSO–SMC–ALADRC deviating from the equilibrium position are 1.477, 2.311, and 0.201 mm, respectively, as shown in Figure 8(c). IPSO–SMC–ALADRC reduces the distance from the equilibrium position by 86.39% and 91.30% compared with PID and LADRC, respectively. Figure 8(d) shows that the control voltage fluctuations of PID, LADRC, and IPSO–SMC–ALADRC were 0.234, 0.672, and 0.156 V after adding 10 N interference, respectively. The fluctuation amplitude of IPSO–SMC–ALADRC's control voltage after

Table 2: Controller parameters in simulation analysis.

Controller	Parameter	Value	Parameter	Value
PID	k_p	1,245.6532	k_i	256.3254
	k_d	8,569.2224		
LADRC	b_0	6.1245	ω_o	465.2365
	ω_c	46.2652		
IPSO–SMC–ALADRC	b_0	1.2659	k_{d0}	0.0536
	ω_o	1,501.2356	k_p	4.2656
	k_{p0}	1,256.2564	k_d	2.3654
	α	0.0256	ϑ	41.6522
	ζ	31.5157		

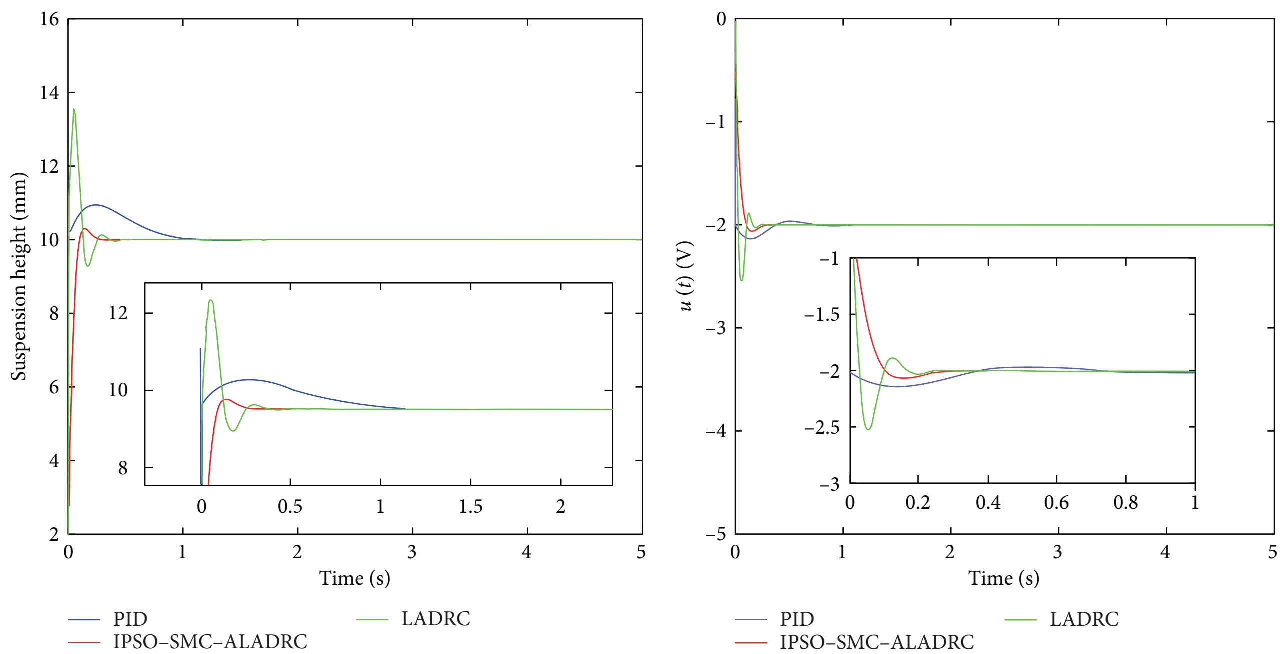

(a) (b)

Figure 6: Step response: (a) suspension height; (b) control voltage.

Table 3: Error index of step response.

Reference signal	Controller	IAE	ITAE	ITSE
Step	PID	4.586×10^{-2}	3.389×10^{-2}	3.120×10^{-3}
	LADRC	2.005×10^{-2}	1.112×10^{-2}	9.989×10^{-4}
	IPSO–SMC–ALADRC	3.021×10^{-3}	4.188×10^{-3}	7.658×10^{-4}

interference decreased by 33.33% and 76.79% compared with those of PID and LADRC, respectively. The simulation results and data levels can prove that IPSO–SMC–ALADRC has excellent anti-interference performance, and the greater the interference intensity, the more evident the superiority of IPSO–SMC–ALADRC's anti-interference ability.

Table 4 illustrates that the error indicators of IAE, ITAE, and ITSE of IPSO–SMC–ALADRC decreased by 94.55%, 93.83%, and 79.49% compared with those of PID when the interference load is 5 N, respectively. The error indicators of IAE, ITAE, and ITSE of IPSO–SMC–ALADRC have decreased by 90.89%, 84.01%, and 16.38% compared with that of LADRC, respectively. When the disturbance load is 10 N, the IAE, ITAE, and ITSE error indicators of IPSO–SMC–ALADRC are decreased by 94.84%, 95.57%, and 84.28% compared with those of PID, respectively. The IAE, ITAE, and ITSE error indicators of IPSO–SMC–ALADRC are reduced by 92.04%, 89.36%, and 23.24% compared with those of LADRC, respectively,

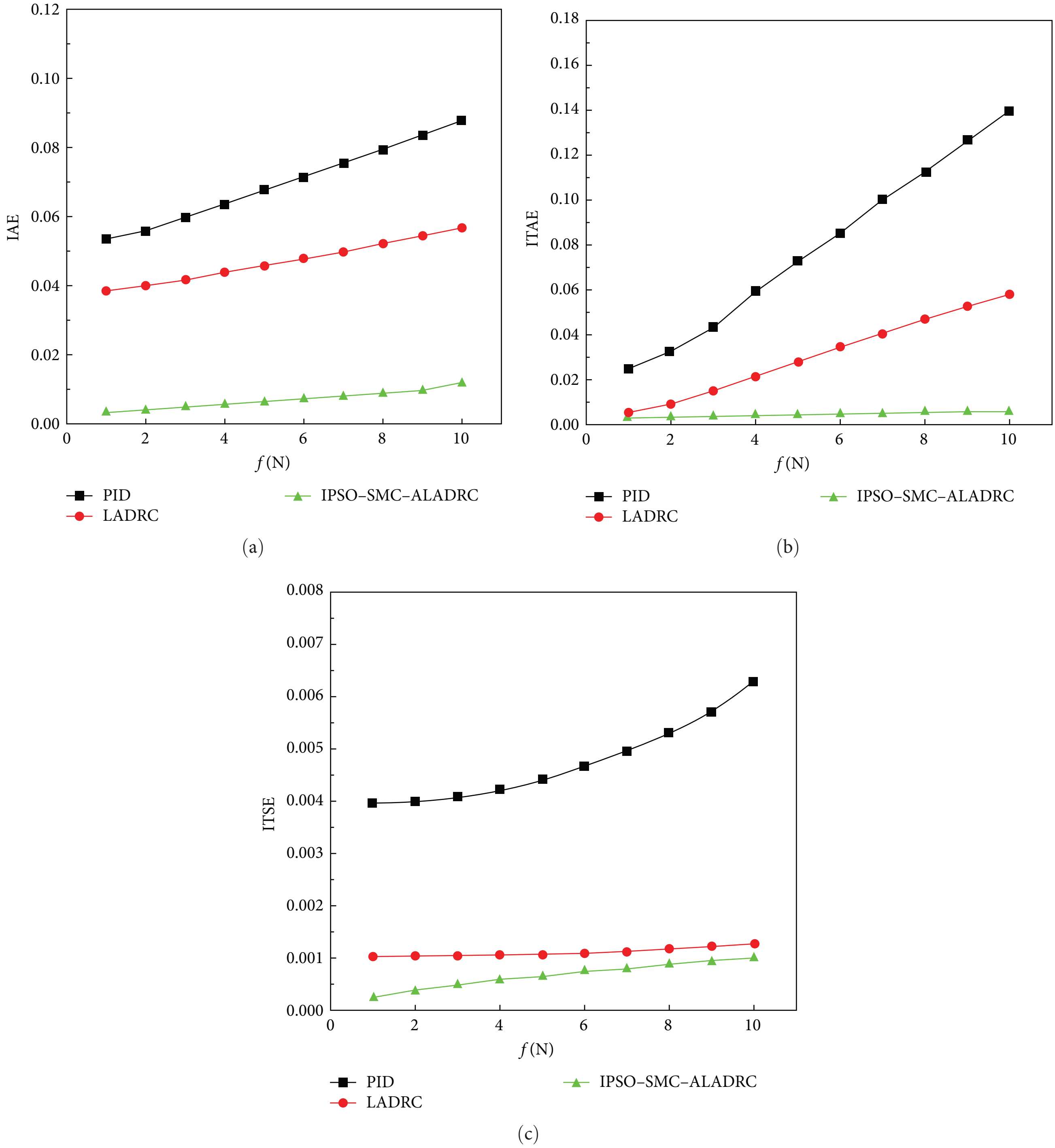

Figure 7: Comparison of errors between PID LADRC and IPSO–SMC–ALADRC under interference changes: (a) trends in IAE error indicators; (b) trends in ITAE error indicators; (c) trends in ITSE error indicators.

indicating that IPSO–SMC–ALADRC has better dynamic performance and robustness.

5. Experimental Verification

The hardware part of the experiment platform is composed of the STM32F10 embedded system, A/D module, steel ball, computer control terminal, laser sensor, drive module, and electromagnet. In terms of software, vofa is used for waveform display, and Keil uvision5 is utilised for programming. The experimental equipment samples at a frequency of 1,000 Hz. The specific experimental equipment is shown in Figure 9.

HG-C1100 is the laser displacement sensor used in this experimental platform. This type of sensor can measure the distance of objects without contact and exhibits the

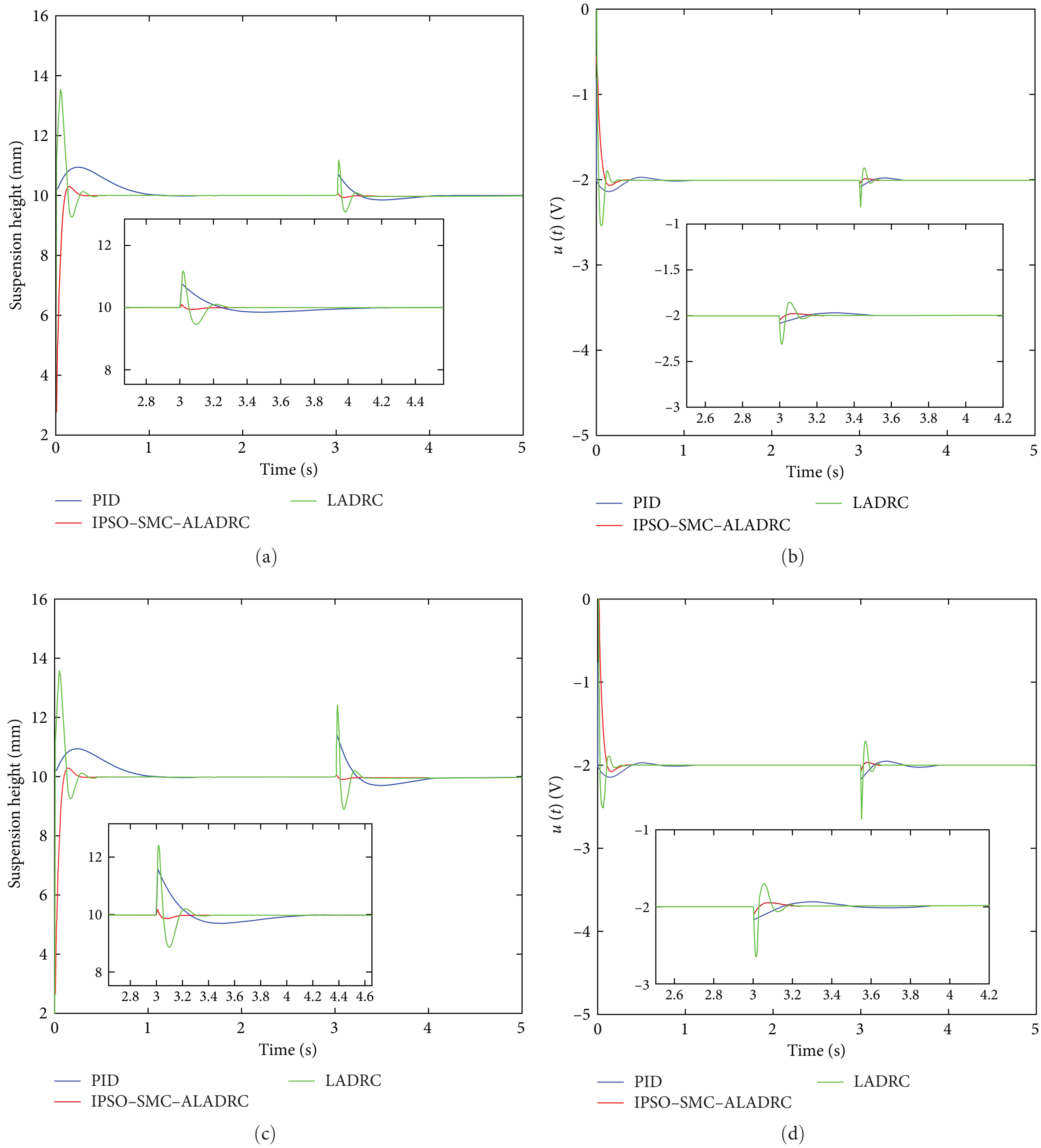

Figure 8: Dynamic disturbance testing of three control methods: (a) suspension height after adding 5 N interference; (b) control voltage after adding 5 N interference; (c) suspension height after adding 10 N interference; (d) control voltage after adding 10 N interference.

characteristics of high accuracy, large range, and strong anti-interference ability. The working principle of the experimental platform is as follows: The A/D module is used to convert the position signal of the steel ball into the initial control voltage. The control voltage is imported into the computer control terminal through the embedded system. The control variable is calculated by the control algorithm in the computer control terminal. Moreover, the control variable is transformed from the form of voltage to the driving current through the drive module, and the driving current is inputted to the electromagnet. The steel ball overcomes its own gravity through the electromagnetic suction generated by the electromagnetic field, thereby achieving suspension.

Here, we selected step signal $y_r = 10$ mm as the input signal for experimental verification of three control methods. At the sixth second, a 4 g magnet was added below the steel ball as a load interference to conduct interference testing.

Table 4: Error index of step response with interference.

Reference signal	Controller	IAE	ITAE	ITSE
Step + interference (5 N)	PID	6.788×10^{-2}	7.326×10^{-2}	4.427×10^{-3}
	LADRC	4.065×10^{-2}	2.833×10^{-2}	1.086×10^{-3}
	IPSO–SMC–ALADRC	3.702×10^{-3}	4.521×10^{-3}	9.081×10^{-4}
Step + interference (10 N)	PID	8.784×10^{-2}	1.403×10^{-1}	6.295×10^{-3}
	LADRC	5.693×10^{-2}	5.839×10^{-2}	1.289×10^{-3}
	IPSO–SMC–ALADRC	4.531×10^{-3}	6.210×10^{-3}	9.895×10^{-4}

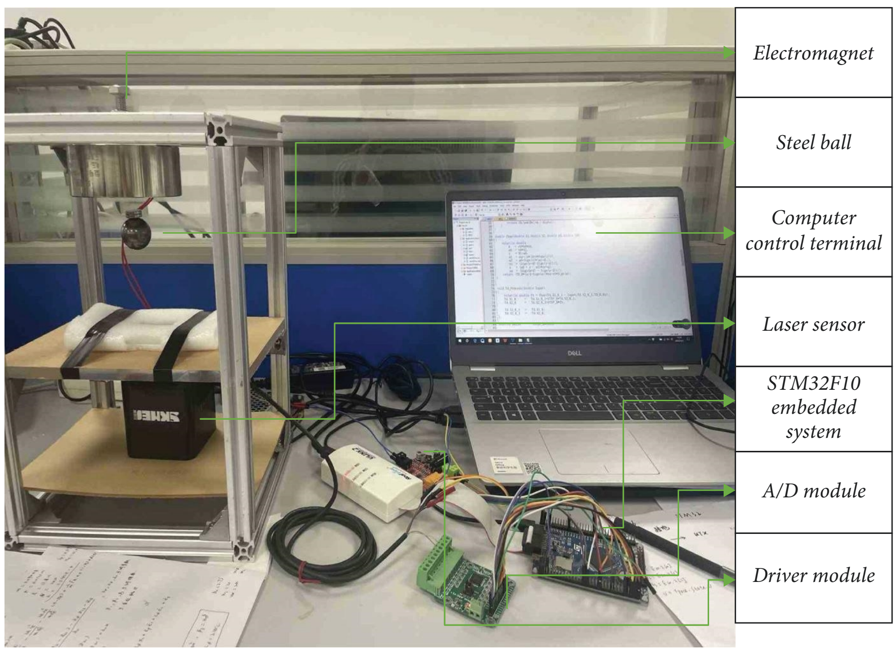

Figure 9: Single-point magnetic levitation ball platform.

Table 5: Controller parameters in experimental verification.

Controller	Parameter	Value	Parameter	Value
PID	k_p	1,245.6532	k_i	256.3254
	k_d	12,000		
LADRC	b_0	4	ω_o	465.2365
	ω_c	46.2652		
IPSO–SMC–ALADRC	b_0	4	k_{d0}	0.0536
	ω_o	1,800	k_p	4.2656
	k_{p0}	1,256.2564	k_d	2.3654
	α	0.0256	ϑ	41.6522
	ζ	31.5157		

The controller parameters verified by experiments are not completely consistent with those analysed by simulation due to the simplification of the controlled object model in simulation analysis. Accordingly, the actual system control parameters must be adjusted and optimised based on the simulation parameters. The experimental parameters of each controller are shown in Table 5.

5.1. PID Control Effect. Figure 10(a) shows that PID can achieve the suspension of steel balls. However, the error between its actual suspension height and the set suspension height fluctuates within ±0.640 mm, and severe shaking occurs during the actual control process. Figure 10(b) demonstrates that the error between the actual control voltage of the PID and the expected control voltage fluctuates

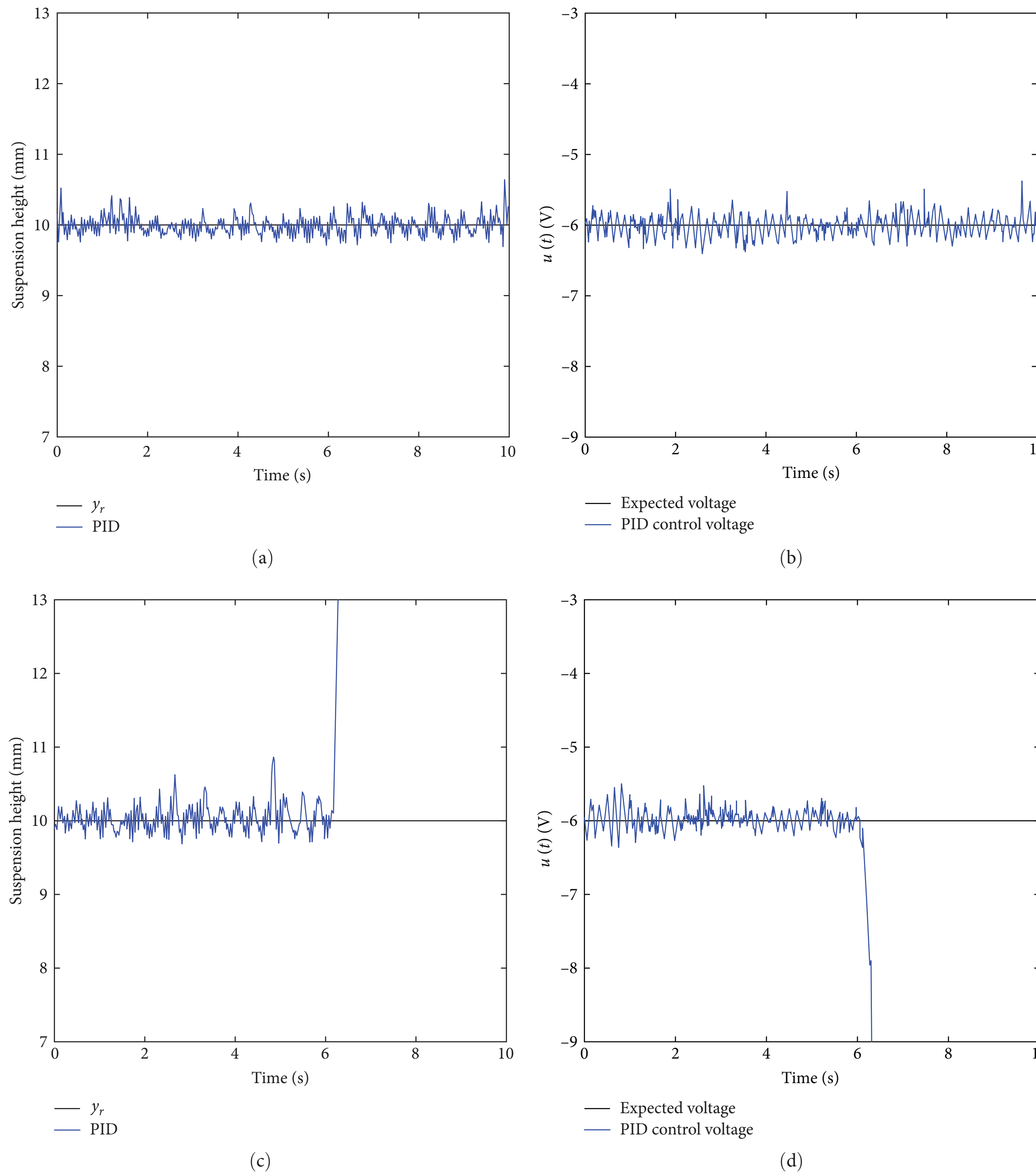

FIGURE 10: PID experimental effect: (a) suspension height without interference; (b) control voltage without interference; (c) suspension height after adding interference; (d) control voltage after adding interference.

within the range of ± 0.631 V without interference. Figure 10(c) shows that after the 4 g load interference was added at the sixth second, the steel ball fell out of control and could not recover to the equilibrium level. Figure 10(d) demonstrates that the actual control voltage of the PID loses control and cannot recover to the expected control voltage after adding interference.

5.2. LADRC Control Effect. Figure 11(a) shows that magnetic levitation can achieve levitation under the control of LADRC. Nevertheless, the error between the actual levitation height and the set levitation height fluctuates within the range of ± 0.632 mm, resulting in significant shaking during the actual control process. Figure 11(b) shows that the error between the actual control voltage and the expected voltage

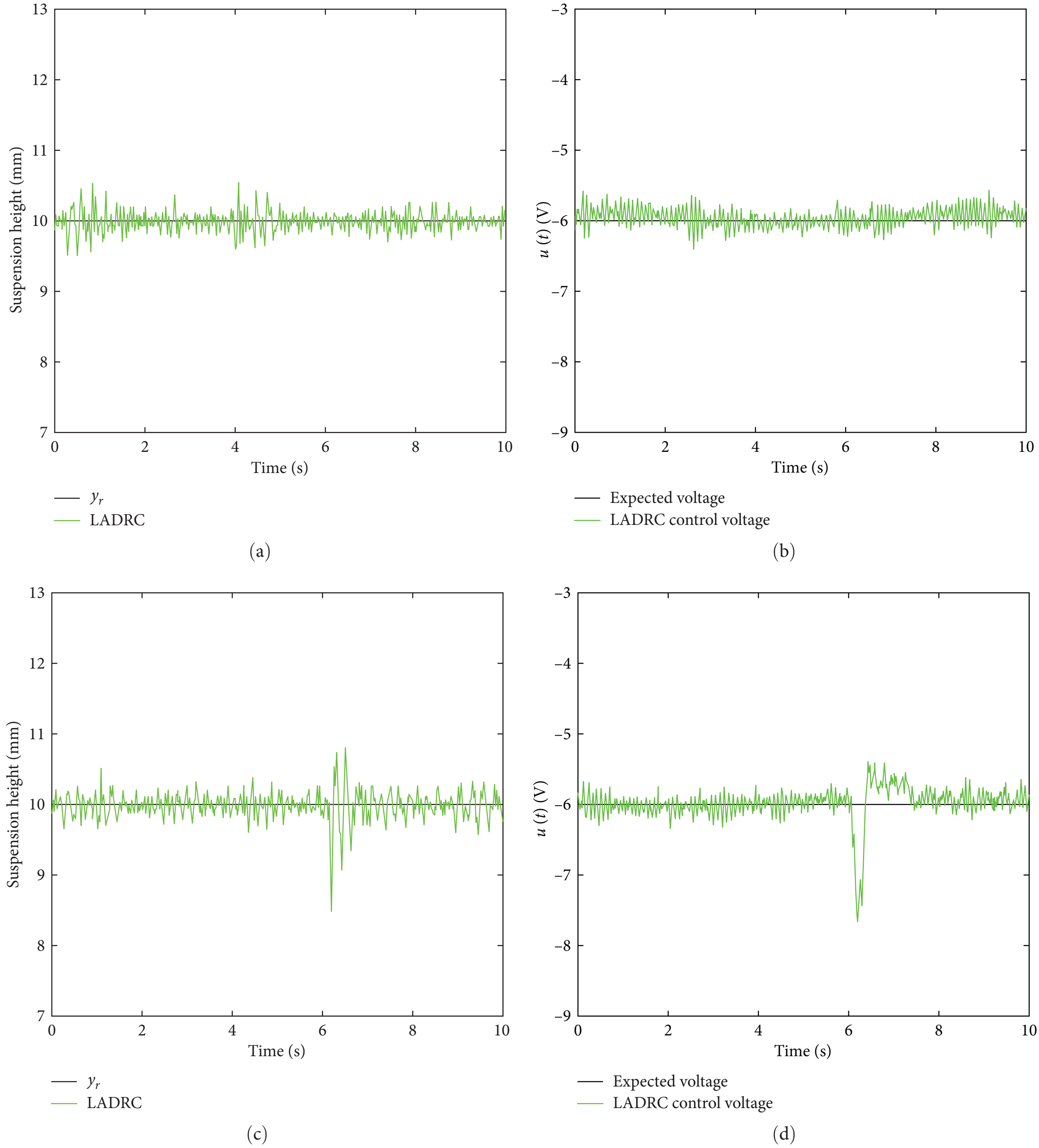

FIGURE 11: LADRC experimental effect: (a) suspension height without interference; (b) control voltage without interference; (c) suspension height after adding interference; (d) control voltage after adding interference.

of LADRC fluctuates within the range of ± 0.432 V without adding interference. Figure 11(c) depicts that under the control of LADRC, the steel ball was subjected to load interference at the sixth second, without any loss of control and falling. However, the actual suspension height had a significant error from the set suspension height, reaching 1.475 mm. Figure 11(d) shows that the fluctuation amplitude of the LADRC control voltage is 1.741 V after adding interference.

5.3. IPSO–SMC–ALADRC Control Effect. Figure 12(a) shows that the magnetic levitation ball has achieved levitation control under the control of IPSO–SMC–ALADRC. The error between the actual levitation height and the set levitation

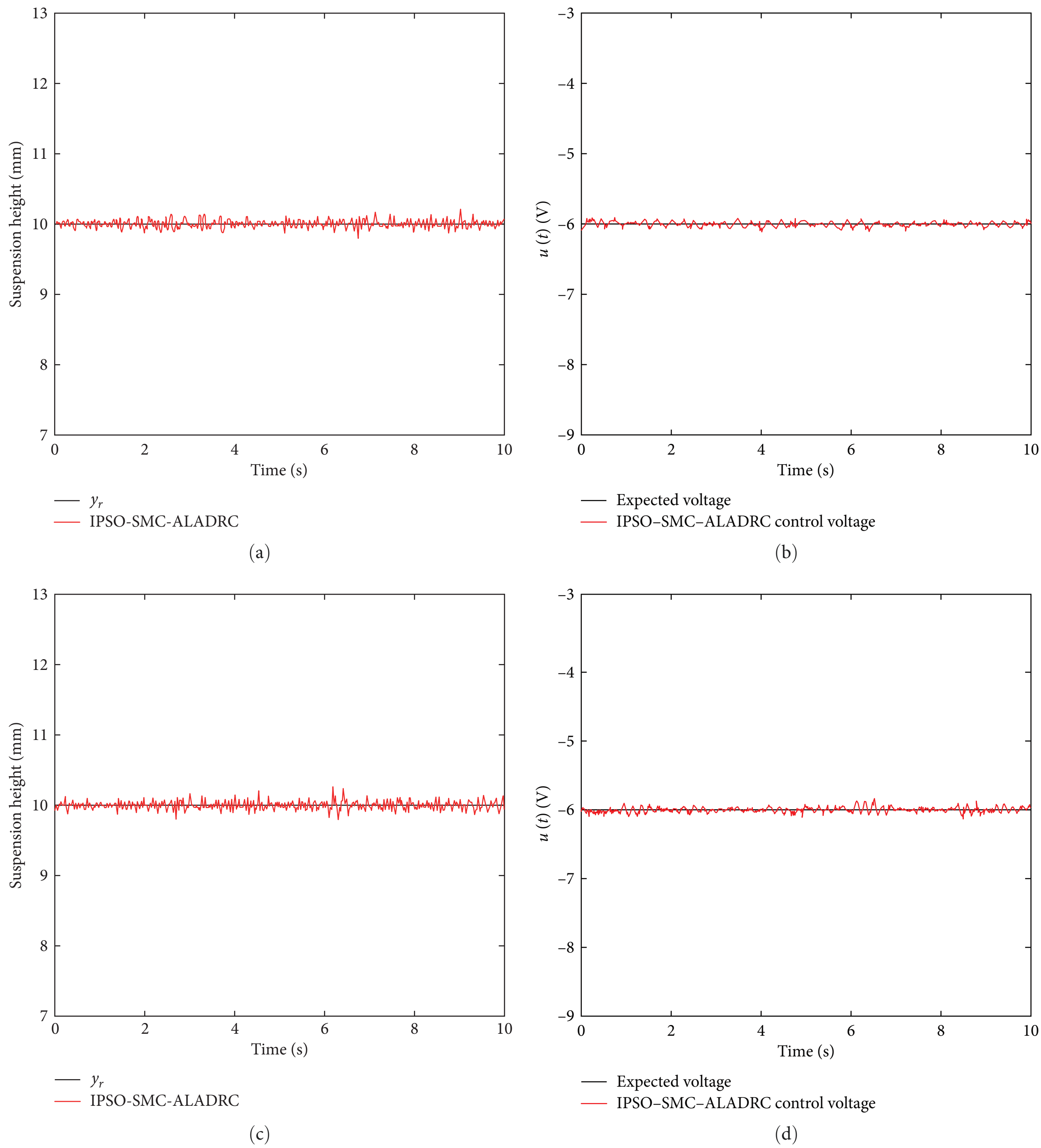

Figure 12: IPSO–SMC–ALADRC experimental effect: (a) suspension height without interference; (b) control voltage without interference; (c) suspension height after adding interference; (d) control voltage after adding interference.

height fluctuates within ± 0.203, which is within a reasonable range, and no significant shaking phenomenon occurred during the actual control process. Figure 12(b) shows that the error between the actual control voltage and the expected voltage of IPSO–SMC–ALADRC fluctuates within the range of ± 0.147 V without interference. Figure 12(c) depicts that the magnetic levitation ball was subjected to a load interference of 4 g at the sixth second, without any loss of control and falling, under the control of IPSO–SMC–ALADRC. Only slight fluctuations occurred, and the actual levitation height was only 0.384 mm away from the set levitation height. In Figure 12(d), the control voltage fluctuation amplitude of IPSO–SMC–ALADRC is 0.232 V after adding interference.

Table 6: Experimental error data for three control methods.

Controller	Error of suspension height (mm)	Interference error of suspension height (mm)	Error of control voltage (V)	Interference error of control voltage (V)
PID	±0.640	–	±0.631	–
LADRC	±0.632	1.475	±0.432	1.741
IPSO–SMC–ALADRC	±0.203	0.384	±0.147	0.232

In summary, regardless of whether interference is added or not, the error of IPSO–SMC–ALADRC is smaller than that of PID and LADRC. In comparison with the non-interference PID and LADRC, the actual suspension height and set suspension height errors of IPSO–SMC–ALADRC decreased by 68.28% and 67.88%, respectively. In terms of control voltage, the actual control voltage and expected voltage errors of IPSO–SMC–ALADRC decreased by 76.70% and 65.97% compared with those of PID and LADRC, respectively. After adding interference, the magnetic levitation ball lost control and fell off under PID control, unable to recover to the set levitation height. The fluctuation displacement of IPSO–SMC–ALADRC decreased by 73.97% compared with that of LADRC. In terms of control voltage, the fluctuation amplitude of IPSO–SMC–ALADRC's control voltage decreased by 86.67% compared with that of LADRC. The specific experimental values are shown in Table 6.

6. Conclusions

This study focuses on the problem of the weak anti-interference ability of traditional control methods in the application of magnetic levitation ball systems and investigates the single-point magnetic levitation ball system. A mathematical model of a single-point magnetic levitation ball was established by ignoring the high-order term of the balance point of the magnetic levitation ball. The PSO was used to adjust the controller parameters in combination with sliding mode and adaptive linear active disturbance rejection. The anti-interference and stability of the three control methods were simulated and verified. The results showed that IPSO–SMC–ALADRC has strong stability. IPSO–SMC–ALADRC reduces the error indicators compared with PID and LADRC, indicating that it has better dynamic performance.

(1) After improvement, the PSO algorithm has higher convergence speed and search accuracy, and the number of iterations required for convergence decreased by 50%.

(2) When IPSO was used to determine the parameters of the three control modes, the fitness value of IPSO–SMC–ALADRC decreased by 87.64% and 62.34% compared with those of PID and LADRC, respectively, reflecting that it has better dynamic performance.

(3) Although PID and LADRC have fast response speeds when the input signal is a step signal, they also generate excessive overshoot loads. Only IPSO–SMC–ALADRC addressed the contradiction between super harmonic and response speed. The adjustment times of PSO–SMC–ALADRC decreased by 82.63% and 46.52% compared with those of PID and LADRC, respectively.

(4) After being disturbed, the LADRC and PID control experienced significant fluctuations and took a significant amount of time to recover to the equilibrium position. Only IPSO–SMC–ALADRC experienced slight fluctuations after being disturbed and quickly recovered to its equilibrium position. When the interference is 5 N, the fluctuation distance of IPSO–SMC–ALADRC decreased by 85.37% and 84.13% compared with those of PID and LADRC, respectively. When the interference was 10 N, the fluctuation distance of IPSO–SMC–ALADRC decreased by 86.39% and 91.30% compared with those of PID and LADRC, respectively. The stronger the interference, the more evident the anti-interference performance advantage of IPSO–SMC–ALADRC.

(5) In the validation of the magnetic levitation ball experimental platform, regardless of whether interference is added, the error of the magnetic levitation ball under IPSO–SMC–ALADRC control is much smaller than that of PID and LADRC. Without adding interference, the errors between the actual suspension height and the ideal suspension height of IPSO–SMC–ALADRC were reduced by 68.28% and 67.88% compared with those of PID and LADRC, respectively. After adding interference, the PID shows uncontrollable detachment and cannot recover to the ideal suspension height. The fluctuation displacement of IPSO–SMC–ALADRC after interference decreased by 73.97% compared with that of LADRC.

We will refer to literatures [36–38] in the next stage to optimise the controller using butterfly optimisation algorithm, gray wolf algorithm, and whale optimisation algorithm. We will further enhance the theoretical analysis of the article and enrich the research content.

Data Availability

The experimental data used to support the findings of this study are available from the corresponding author upon request.

Conflicts of Interest

The authors declare that they have no conflicts of interest.

Acknowledgments

This research was funded by the Central Guided Local Science and Technology Funding Project of the Science and Technology Department of Jiangxi Province (Cross-regional Cooperation, 20221ZDH04052), the 03 Special Project and 5G Program of the Science and Technology Department of Jiangxi Province (no. 20193ABC03A058), the Program of Qingjiang Excellent Young Talents in Jiangxi University of Science and Technology (no. JXUSTQJBJ2019004), and this work was supported by the Key Research and Development Plan of Ganzhou (industrial field) (No. (2019)60), a grant from the Research Projects of Ganjiang Innovation Academy, Chinese Academy of Sciences (no. E255J001), and the cultivation project of the State Key Laboratory of Green Development and High-Value Utilization of Ionic Rare-Earth Resources in Jiangxi Province (no. 20194AFD44003), supported by Jiangxi Provincial Natural Science Foundation (no. 20232ACB202001).

References

[1] W. X. Liu, W. L. Li, and J. Fang, "Review of research on high temperature maglev," *Cryogenics & Superconductivity*, vol. 48, no. 2, pp. 44–49, 2020.

[2] W. C. Wang, X. G. Chu, W. X. Wang, and S. Rui, "Two degree of freedom magnetic levitation ball control based on sliding mode state observer," *Engineering College of Qufu Normal University*, vol. 13, pp. 355–362, 2021.

[3] Z. Guan and T. Yamamoto, "Design of a reinforcement learning PID controller," in *2020 International Joint Conference on Neural Networks (IJCNN)*, pp. 1–6, IEEE, Glasgow, UK, 2020.

[4] X. J. Su, X. Z. Yang, and P. Shi, "Fuzzy control of nonlinear electromagnetic suspension systems," *Mechatronics*, vol. 24, no. 4, pp. 328–335, 2014.

[5] J. Yang, H. Shi, H. L. Hu, and C. Huang, "ADRC algorithm for single-point suspension system," *Journal of Ordnance Equipment Engineering*, vol. 41, no. 4, pp. 167–171, 2020.

[6] Q. H. Gao, H. Yan, H. X. Zou et al., "Magnetic levit-ation using diamagnetism: mechanism, applications and prospects," *Science China Technological Sciences*, vol. 64, no. 1, pp. 44–58, 2021.

[7] Y. Y. Shi, X. F. Peng, Q. L. Feng, and J. K. Sha, "High overload maneuver control of ramjet missile based on active disturbance rejection control," *Journal of Ordnance Equipment Engineering*, vol. 42, no. 7, pp. 13–18, 2021.

[8] Q. Ouyang, K. Fan, Y. Liu, and N. Li, "Adaptive LADRC parameter optimization in magnetic levitation," in *IEEE Access*, vol. 9, pp. 36791–36801, 2021.

[9] J. G. Yu and B. L. Mu, "Research on optimization of suspension control based on LADRC," *Journal of Railway Science and Engineering*, vol. 19, no. 12, pp. 3477–3483, 2022.

[10] Z. X. Su, J. Yang, Y. Peng, and F. Peng, "Simulating active disturbance-resistant control of single-point hybrid magnetic," *Journal of Railway Science and Engineering*, vol. 19, no. 4, pp. 864–873, 2022.

[11] L. B. Wei, K. G. Fan, X. H. Zhou, L. F. Hu, and W. G. Tang, "Linear active disturbance rejection control of magnetic levitation system based on cuckoo search," in *2022 IEEE 11th Data Driven Control and Learning Systems Conference (DDCLS)*, pp. 151–157, Chengdu, China, 2022.

[12] O. Qinghua, F. Kuangang, and L. Shuang, "Research on adaptive radial basis function control method of magnetic levitation ball," *Journal of Railway Science and Engineering*, pp. 1–11, 2023.

[13] J. Yang, C. Huang, and S. Heng, "Adaptive sliding mode control for suspension height of the suspended ball based on RBF neural network compensation," *Electrical technology*, vol. 21, no. 2, pp. 26–30, 2020.

[14] D. Ma, M. Song, P. Yu, and J. Li, "Research of RBF-PID control in maglev system," *Symmetry*, vol. 12, no. 11, pp. 1780–1788, 2020.

[15] W. Yang, F. Meng, S. Meng, S. Man, and A. Pang, "Tracking control of magnetic levitation system using model-free RBF neural network design," *IEEE Access*, vol. 8, pp. 204563–204572, 2020.

[16] C.-L. Zhang, X.-Z. Wu, and J. Xu, "Particle swarm sliding mode-fuzzy PID control based on maglev system," *IEEE Access*, vol. 9, pp. 96337–96344, 2021.

[17] X. J. Wang, L. J. Chen, and L. Yu, "Model predictive control for magnetic levitation ball system based on equivalent input disturbance sliding mode observer," *Control Theory & Applications*, vol. 38, no. 1, pp. 137–146, 2021.

[18] X. L. Shen, X. Mo, and Y. N. Zhou, "Magnetic levitation ball position control research based on fuzzy neural network," *Agricultural Equipment & Vehicle Engineering*, vol. 56, no. 5, pp. 59–64, 2018.

[19] Z. Wei, Z. Huang, and J. Zhu, "Position control of magnetic levitation ball based on an improved AdaGrad algorithm and deep neural network feedforward compensation control," *Mathematical Problems in Engineering*, vol. 2020, Article ID 8935423, 13 pages, 2020.

[20] Y. Sun, J. Xu, G. Lin, W. Ji, and L. Wang, "RBF neural network-based supervisor control for maglev vehicles on an elastic track with network time delay," in *IEEE Transactions on Industrial Informatics*, vol. 18, no. 1, pp. 509–519, 2022.

[21] Y. Sun, J. Xu, H. Qiang, C. Chen, and G. B. Lin, "Adaptive sliding mode control of maglev system based on RBF neural network minimum parameter learning method," *Measurement*, vol. 141, pp. 217–226, 2019.

[22] Y. Sun, J. Xu, H. Qiang, and G. Lin, "Adaptive neural-fuzzy robust position control scheme for maglev train systems with experimental verification," *IEEE Transactions on Industrial Electronics*, vol. 66, no. 11, pp. 8589–8599, 2019.

[23] Z. G. Lv and Z. Q. Long, "Method on nonlinear adaptive controller for maglev levitation ball system," *Control Engineering of China*, vol. 27, no. 1, pp. 127–133, 2020.

[24] D.-G. Gao, Y.-G. Sun, S.-H. Luo, G.-B. Lin, and L.-S. Tong, "Deep learning controller design of embedded control system for maglev train via deep belief network algorithm," *Design Automation for Embedded Systems*, vol. 24, no. 3, pp. 161–181, 2020.

[25] A. Fatemimoghadam, H. Toshani, and M. Manthouri, "Control of magnetic levitation system using recurrent neural network-based adaptive optimal backstepping strategy," *Transactions of the Institute of Measurement and Control*, vol. 42, no. 13, pp. 2382–2395, 2020.

[26] B. E. Silva and R. S. Barbosa, "Experiments with neural networks in the identification and control of a magnetic levitation system using a low-cost platform," *Applied Sciences*, vol. 11, no. 6, pp. 2535–2541, 2021.

[27] B. L. Li, L. Zeng, P. M. Zhang, and Z. D. Zhu, "Backstepping control of maglev ball based on extended state observer," *Journal of Hebei University of Science and Technology*, vol. 42, no. 2, pp. 144–151, 2021.

[28] L. L. Liu and J. H. Zuo, “Fuzzy PID parameter self-adjusting control method for maglev ball system,” *Control Engineering*, vol. 28, no. 2, pp. 354–359, 2021.
[29] S. Y. Gong and D. Li, “Fuzzy reinforcement learning control of maglev ball system based on particle swarm optimization,” *Shihezi Science and Technology*, vol. 2021, no. 1, pp. .41–43, 2021.
[30] J. de Jesús Rubio, L. Zhang, E. Lughofer, P. Cruz, A. Alsaedi, and T. Hayat, “Modeling and control with neural networks for a magnetic levitation system,” *Neurocomputing*, vol. 227, pp. 113–121, 2017.
[31] X. Zhou, C. Yang, B. Zhao, L. Zhao, and Z. Zhu, “A high-precision control scheme based on active disturbance rejection control for a three-axis inertially stabilized platform for aerial remote sensing applications,” *Journal of Sensors*, vol. 2018, Article ID 7295852, 9 pages, 2018.
[32] A. J. Humaidi, H. M. Badr, and A. H. Hameed, “PSO-based active disturbance rejection control for position control of magnetic levitation system,” in *2018 5th International Conference on Control, Decision and Information Technologies (CoDIT)*, pp. 922–928, IEEE, Thessaloniki, Greece, 2018.
[33] A. J. Humaidi and H. M. Badr, “Linear and nonlinear active disturbance rejection controllers for single-link flexible joint robot manipulator based on PSO tuner,” *Journal of Engineering Science and Technology Review*, vol. 11, no. 3, pp. 133–138, 2018.
[34] A. J. Humaidi, H. M. Badr, and A. R. Ajil, “Design of active disturbance rejection control for single-link flexible joint robot manipulator,” in *22nd International Conference on System Theory, Control and Computing (ICSTCC)*, pp. 452–457, IEEE, Sinaia, Romania, 2018.
[35] Z. J. Wang, “Attitude control of quadrotor UAV based on linear active disturbance rejection,” University of Science and Technology, Qingdao, 2023.
[36] A. I. Abdul-Kareem, A. F. Hasan, A. A. AL-Qassar et al., “Rejection of wing-rock motion in delta wing aircrafts based on optimal ladrc schemes with butterfly optimization algorithm,” *Journal of Engineering Science and Technology*, vol. 17, no. 4, pp. 2476–2495, 2022.
[37] A. L. Q. Arif, A. A. Ibraheem, H. Alaq et al., “Grey-wolf optimization better enhances the dynamic performance of roll motion for tail-sitter VTOL aircraft guided and controlled by STSMC,” *Journal of Engineering Science and Technology*, vol. 16, no. 3, pp. 1932–1950,2021.
[38] Z. A. Waheed and A. J. Humaidi, “Design of optimal sliding mode control of elbow wearable exoskeleton system based on whale optimization algorithm,” *Journal Européen des Systèmes Automatisés*, vol. 55, no. 4, pp. 459–466, 2022.